

Contents lists available at ScienceDirect

Journal of Computational Physics

journal homepage: www.elsevier.com/locate/jcp



Robust fast direct integral equation solver for three-dimensional doubly periodic scattering problems with a large number of layers

Bowei Wu, Min Hyung Cho*

Department of Mathematics and Statistics, University of Massachusetts Lowell, 220 Pawtucket St, Lowell, 01854, MA, USA

ARTICLE INFO

Dataset link: https://github.com/bobbielf2/ZetaTrap3D_Unified

Keywords:
Multilayered media
Helmholtz equations
Periodic boundary condition
Green's functions
Boundary integral equations
Numerical integration

ABSTRACT

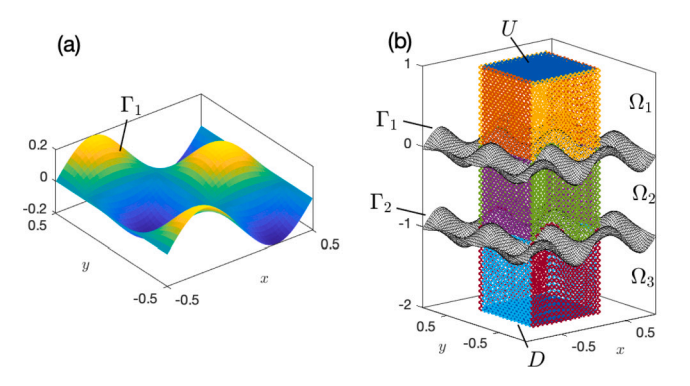
Frequency-domain wave scattering problems that arise in acoustics and electromagnetism can be often described by the Helmholtz equation. This work presents a boundary integral equation method for the Helmholtz equation in 3-D multilayered media with many doubly periodic smooth layers. Compared with conventional quasi-periodic Green's function method, the new method is robust at all scattering parameters. A periodizing scheme is used to decompose the solution into near- and far-field contributions. The near-field contribution uses the free-space Green's function in an integral equation on the interface in the unit cell and its immediate eight neighbors; the far-field contribution uses proxy point sources that enclose the unit cell. A specialized high-order quadrature is developed to discretize the underlying surface integral operators to keep the number of unknowns per layer small. We achieve overall linear computational complexity in the number of layers by reducing the linear system into block tridiagonal form and then solving the system directly via block LU decomposition. The new solver is capable of handling a 100-interface structure with 961.3k unknowns to 10^{-5} accuracy in less than 2 hours on a desktop workstation.

1. Introduction

Optical or electromagnetic waves in doubly periodic multilayered media is one of the fundamental mechanisms in many modern high-tech devices such as dielectric gratings for high-powered laser [1,2], thin-film photovoltaic [3,4], passive cooling devices using multilayer photonic structure [5], photonic crystals [6], semiconductor packaging that is one of the hot topics in chip design [7,8], and process control in semiconductor lithography [9]. Numerical simulations are often used to help design or optimize these devices where one must solve the scattering problem for various incident angles and/or wavelengths and repeat the computation for design optimization in many cases [10]. Therefore, it is imperative to have a robust and efficient solver. There are many well-known numerical methods, including finite-difference time-domain method [11], finite element method [12–14], rigorous-coupled wave analysis or Fourier modal method [15–17], high-order perturbation of surface (HOPS) method [18,19], and integral equation method [20–31]. Each method has its own advantages and disadvantages. The integral equation method stands out with several very attractive benefits over other methods: the dimensionality of the problem is reduced with all the unknowns residing on the interfaces instead of in the volume, which significantly reduces the number of unknowns; the radiation condition is built into the Green's function and no artificial boundary conditions or perfectly matched layers are required; moreover, a problem can often be formulated as a Fredholm second-kind integral equation which is well-conditioned and suitable for an accelerated iterative matrix

^{*} Corresponding author.

E-mail address: minhyung_cho@uml.edu (M.H. Cho).



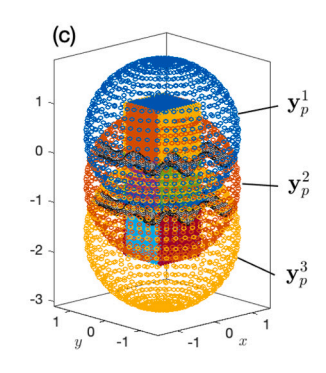


Fig. 1. (a) An interface parameterized by $g(x, y) = 0.2 \sin(2\pi x) \cos(2\pi y)$, with period d = 1 in both directions. (b) Structure with multiple interfaces Γ_i with the surrounding walls for each layer Ω_i . (c) Proxy points $\{y_{i,j}^*\}$ on spheres enclosing each layer Ω_i .

solver. However, due to the nature of the Green's function, discretization of the integral equation usually yields a dense matrix that is expensive to invert directly. Thus, large system solvers must be accelerated using fast linear algebra algorithms, such as the Fast Multipole Method [32–34] and the Fast Direct Solver [35–39].

The focus of the present paper is on the frequency-domain scattering of a plane wave through a stratified medium with many layers which has applications in acoustic waves such as acoustic metamaterials [40,41]. For two dimensional (2-D) doubly periodic multilayered media, the boundary integral equation method combined with a periodizing scheme is used to build an efficient solver that can handle 1000 s of layers [27]. The solver is further accelerated by the fast direct solver recently developed by Zhang and Gillman [28,29] which can handle complex interfaces that require a large number of samples and is useful for parameter optimization. For three-dimensional (3-D) problems, to avoid challenges of surface integral quadrature, the Method of fundamental solution (MFS) has been used in the place of boundary integral equation for doubly periodic multilayered media [30,31] and for doubly periodic arrays of axisymmetric objects [42]. However, the MFS approach has many limitations associated with the choice of artificial source points near the boundary and the ill-conditioning of the linear system, making it impractical as a general solver even though it was a good tool to show the effectiveness of the periodizing scheme in three dimensions. The difficulty of singular quadrature on layer interfaces has finally been overcome thanks to the recent development of the corrected trapezoidal quadrature [43–45]. The present paper presents a robust and fast integral equation solver for the Helmholtz equation in 3-D doubly periodic smooth multilayered media using the direct solver based on Schur complement and block tridiagonal LU decomposition that was used for the 2-D problem [27]. One review paper [46] from the year 2015 named the authors as one of the groups potentially capable of efficiently solving 3-D scattering or diffraction problems using a boundary integral equation method. Similar to the 2-D solver, the new 3-D solver's CPU time grows linearly with number of layers and is robust at Wood anomalies [47], making it possible to handle a large number of layers. In addition, this solver can be made highly efficient for optimization problems once it is accelerated by a fast direct solver that is a 3-D extension of [29]; results of such an accelerated solver will be reported in a future work.

The geometry of the problems (See Fig. 1 for notation and schematics) consists of I+1 layers denoted by $\{\Omega_i\}_{i=1}^{I+1}$. There are I surfaces $\{\Gamma_i\}_{i=1}^I$ where Γ_i is the interface that separates Ω_i and Ω_{i+1} . For simplicity, all interfaces are assumed to have the same periodicity d along x- and y-directions (see Fig. 1(b)); however, all the following derivations can be easily adapted to interfaces with different periodicities along the two directions (such as modifying the Bloch phases in (3) accordingly). The wavenumber is $\{k_i\}_{i=1}^{I+1}$ in each layer. L_i , R_i , F_i , and B_i are the artificial side walls surrounding the unit cell of the layer Ω_i to impose quasi-periodic boundary conditions. U and D are, respectively, the artificial layers placed above Γ_1 at $z=z_u$ and below Γ_I at $z=z_d$ to impose the radiation conditions. A plane wave is incident in the uppermost layer,

$$u^{\text{inc}}(\mathbf{r}) = \begin{cases} e^{i\mathbf{k}\cdot\mathbf{r}}, & \mathbf{r} \in \Omega_1, \\ 0, & \text{otherwise,} \end{cases}$$
 (1)

where the wave vector

$$\mathbf{k} = (k_{1x}, k_{1y}, k_{1z}) = (k_1 \sin \phi^{\text{inc}} \cos \theta^{\text{inc}}, k_1 \sin \phi^{\text{inc}} \sin \theta^{\text{inc}}, k_1 \cos \phi^{\text{inc}})$$

with $0 \le \theta^{\rm inc} < 2\pi$ and $\pi/2 < \phi^{\rm inc} < \pi$, and where $\mathbf{r} = (x, y, z)$. The incident wave is quasi-periodic (periodic up to a phase) in both directions, that is

$$a_{x}^{-1}u^{\text{inc}}(x+d,y,z) = a_{y}^{-1}u^{\text{inc}}(x,y+d,z) = u^{\text{inc}}(x,y,z),$$
(2)

where the Bloch phases α_x and α_y are defined by

$$\alpha_x = e^{idk_{1x}}$$
 and $\alpha_y = e^{idk_{1y}}$. (3)

From the standard scattering theory [48], the scattered wave u_i must be quasi-periodic and satisfy the Helmholtz equation. Thus, the boundary value problem (BVP) for u_i consists of the equation

$$\Delta u_i(\mathbf{r}) + k_i^2 u_i(\mathbf{r}) = 0, \ \mathbf{r} \in \Omega_i$$
(4)

the continuity conditions at each interface Γ_i , $i = 1, 2, \dots I$

$$u_{1} - u_{2} = -u^{\text{inc}} \quad \text{and} \quad \frac{\partial u_{1}}{\partial \mathbf{n}} - \frac{\partial u_{2}}{\partial \mathbf{n}} = -\frac{\partial u^{\text{inc}}}{\partial \mathbf{n}} \quad \text{on } \Gamma_{1}$$

$$u_{i} - u_{i+1} = 0 \quad \text{and} \quad \frac{\partial u_{i}}{\partial \mathbf{n}} - \frac{\partial u_{i+1}}{\partial \mathbf{n}} = 0 \quad \text{on } \Gamma_{i}, i = 2, 3, \dots, I$$
(5)

the quasi-periodicity conditions on the side walls for all layers

$$u_i|_{L_i} = \alpha_x^{-1} u_i|_{R_i} \quad \text{and} \quad u_i|_{B_i} = \alpha_y^{-1} u_i|_{F_i}$$

$$\frac{\partial u_i}{\partial \mathbf{n}}|_{L_i} = \alpha_x^{-1} \frac{\partial u_i}{\partial \mathbf{n}}|_{R_i} \quad \text{and} \quad \frac{\partial u_i}{\partial \mathbf{n}}|_{B_i} = \alpha_y^{-1} \frac{\partial u_i}{\partial \mathbf{n}}|_{F_i} \quad \text{for } i = 1, 2, \dots I + 1,$$

$$(6)$$

and the upward and downward radiation condition in u_1 and u_{I+1} , respectively, expressed as Rayleigh-Bloch expansions [49]

$$u(\mathbf{r}) = \sum_{m,n} a_{mn}^{\mathbf{u}} e^{i(\kappa_{x}^{m} x + \kappa_{y}^{n} y + k_{\mathbf{u}}^{(m,n)}(z - z_{\mathbf{u}}))}, z \ge z_{\mathbf{u}}$$

$$(7)$$

$$u(\mathbf{r}) = \sum_{m,n} a_{mn}^{d} e^{i(\kappa_{x}^{m} x + \kappa_{y}^{n} y - k_{d}^{(m,n)}(z - z_{d}))}, z \le z_{d},$$
(8)

where $\kappa_x^m = k_{1x} + 2\pi m/d$, $\kappa_y^n = k_{1y} + 2\pi n/d$,

$$k_{\rm u}^{(m,n)} = \sqrt{k_1^2 - (\kappa_{\rm x}^m)^2 - (\kappa_{\rm y}^n)^2}, \text{ and } k_{\rm d}^{(m,n)} = \sqrt{k_{I+1}^2 - (\kappa_{\rm x}^m)^2 - (\kappa_{\rm y}^n)^2},$$

and the sign of the square root is taken as positive real or positive imaginary. It is known that the boundary value problem (4)–(8) has a solution for all parameters and the solution is unique at all but a discrete set of frequencies k and incident angles θ^{inc} that correspond to guided modes of the dielectric structure [49]. However, these should not be confused with Wood anomalies, which are scattering parameters that produce the upper or lower n^{th} Rayleigh-Bloch mode a horizontally traveling wave [50–52].

In Section 2, we describe the periodized boundary integral representation and its discretization for the BVP (4)-(8), where a new specialized quadrature is introduced in Section 2.2. Section 3 describes the fast solution procedure for the discretized system by a reduction into block tridiagonal form. Several numerical examples are presented in Section 4 and the paper is concluded in Section 5.

2. Boundary integral formulation, periodizing scheme, and its discretization

From the periodizing idea in two-dimensions [27], the scattered field or solution of the Helmholtz equation (4) in each layer is represented by the sum of near- and far-field contribution. The near-field contribution uses the free-space Green's function in an integral equation on the interfaces in the unit cell and its 8 immediate neighbors. The far-field contribution uses artificial (proxy) point sources on a sphere that is centered on and enclosing the unit cell.

We first define the standard single- and double-layer potentials [48] for the Helmholtz equation residing on a general surface Γ at wavenumber k_i for the ith layer,

$$(S_{\Gamma}^{i}\sigma)(\mathbf{r}) := \int_{\Gamma} G^{i}(\mathbf{r}, \mathbf{r}')\sigma(\mathbf{r}') \, \mathrm{d}S_{\mathbf{r}'}, \quad (\mathcal{D}_{\Gamma}^{i}\tau)(\mathbf{r}) := \int_{\Gamma} \frac{\partial G^{i}}{\partial \mathbf{n}'}(\mathbf{r}, \mathbf{r}')\tau(\mathbf{r}') \, \mathrm{d}S_{\mathbf{r}'}, \tag{9}$$

where \mathbf{n}' is the unit normal on Γ at \mathbf{r}' , and where

$$G^{i}(\mathbf{r}, \mathbf{r}') := \frac{e^{ik_{i}|\mathbf{r}-\mathbf{r}'|}}{4\pi|\mathbf{r}-\mathbf{r}'|}$$

$$\tag{10}$$

is the free-space Green's function at wavenumber k_i . The normal derivative of the potentials with respect to the unit normal vector \mathbf{n} at the target point \mathbf{r} are defined as

$$(\mathcal{D}_{\Gamma}^{i,*}\tau)(\mathbf{r}) := \int_{\Gamma} \frac{\partial G^{i}}{\partial \mathbf{n}}(\mathbf{r}, \mathbf{r}')\tau(\mathbf{r}') \,\mathrm{d}S_{\mathbf{r}'}, \quad (\mathcal{T}_{\Gamma}^{i}\tau)(\mathbf{r}) := \int_{\Gamma} \frac{\partial^{2} G^{i}}{\partial \mathbf{n}\partial \mathbf{n}'}(\mathbf{r}, \mathbf{r}')\tau(\mathbf{r}') \,\mathrm{d}S_{\mathbf{r}'}. \tag{11}$$

Define the phased contribution from the nearest neighbors (indicated with a tilde)

$$(\tilde{S}_{\Gamma}^{i}\sigma)(\mathbf{r}) := \sum_{\substack{-1 \le I_{x}, I_{y} \le 1\\ \mathbf{d} = d \ (I_{x}, I_{y}, 0)}} \alpha_{x}^{I_{x}} \alpha_{y}^{I_{y}} \int_{\Gamma} G^{i}(\mathbf{r}, \mathbf{r}' + \mathbf{d}) \sigma(\mathbf{r}') \, \mathrm{d}S_{\mathbf{r}'}$$

$$(12)$$

$$(\tilde{\mathcal{D}}_{\Gamma}^{i}\tau)(\mathbf{r}) := \sum_{\substack{1 \le l_{x}, l_{y} \le 1\\ \mathbf{d} = d(l_{x}, l_{y}, 0)}} \alpha_{x}^{l_{x}} \alpha_{y}^{l_{y}} \int_{\Gamma} \frac{\partial G^{i}}{\partial \mathbf{n}'}(\mathbf{r}, \mathbf{r}' + \mathbf{d})\tau(\mathbf{r}') \, \mathrm{d}S_{\mathbf{r}'}.$$

$$(13)$$

The operators $\tilde{\mathcal{D}}_{\Gamma}^{i,*}$ and $\tilde{\mathcal{T}}_{\Gamma}^{i}$ are defined in the same manner. Furthermore, we will use two subscripts to denote target and source interfaces, for example,

R Wu and M H Cho

$$(\tilde{S}_{\Gamma_t,\Gamma_s}^i \sigma)(\mathbf{r}) := \sum_{\substack{1 \le I_x,I_y \le 1 \\ \mathbf{d} = d \ (l_x,I_y,0)}} \alpha_x^{l_x} \alpha_y^{l_y} \int_{\Gamma_s} G^i(\mathbf{r}, \mathbf{r}' + \mathbf{d}) \sigma(\mathbf{r}') \, \mathrm{d}S_{\mathbf{r}'}, \quad \mathbf{r} \in \Gamma_t,$$

$$(14)$$

represents the single layer operation defined in (12) at the target interface Γ_t due to the source interface Γ_s . Other source-target interaction operators, such as $\tilde{\mathcal{D}}^i_{\Gamma_t,\Gamma_s}$, $\tilde{\mathcal{D}}^{i*}_{\Gamma_t,\Gamma_s}$, and $\tilde{\mathcal{T}}^i_{\Gamma_t,\Gamma_s}$ are similarly defined.

Next we let \mathbb{S}_i be the sphere of radius R that is centered on and encloses the domain Ω_i , and define the proxy points $\{\mathbf{y}_p^i\}_{p=1}^P$ to be the uniformly spaced mesh points in the standard longitude-latitude parameterization of \mathbb{S}_i (see Fig. 1(c)). Then the proxy basis functions for the ith layer are

$$\phi_p^i(\mathbf{r}) := \frac{\partial G^i}{\partial \mathbf{n}_p} (\mathbf{r}, \mathbf{y}_p^i) + ik_i G^i(\mathbf{r}, \mathbf{y}_p^i), \quad \mathbf{r} \in \Omega_i, \quad p = 1, \dots, P$$
(15)

where \mathbf{n}_p is the outward-pointing unit normal to \mathbb{S}_i at \mathbf{y}_p^i . The basis functions (15) are chosen to make the proxy representation more robust at higher wavenumbers [27]. The choice of proxy surfaces can also be flexible. For example, one can replace the sphere \mathbb{S}_i with a horizontally stretched ellipsoid when the unit cell Ω_i is very thin along the *z*-direction.

Combining the above definitions of near-field layer potentials and proxy basis, the ansatz for the scattered field in each layer is then given by

$$u_{1}(\mathbf{r}) = \tilde{D}_{\Gamma_{1}}^{I} \tau_{1} + \tilde{S}_{\Gamma_{1}}^{I} \sigma_{1} + \sum_{p=1}^{P} c_{p}^{I} \phi_{p}^{I}, \qquad \mathbf{r} \in \Omega_{1},$$

$$u_{i}(\mathbf{r}) = \tilde{D}_{\Gamma_{i-1}}^{I} \tau_{i-1} + \tilde{S}_{\Gamma_{i-1}}^{I} \sigma_{i-1} + \tilde{D}_{\Gamma_{i}}^{I} \tau_{i} + \tilde{S}_{\Gamma_{i}}^{I} \sigma_{i} + \sum_{p=1}^{P} c_{p}^{I} \phi_{p}^{I}, \qquad \mathbf{r} \in \Omega_{i}, i = 2, 3, \dots I,$$

$$u_{I+1}(\mathbf{r}) = \tilde{D}_{\Gamma_{I}}^{I+1} \tau_{I} + \tilde{S}_{\Gamma_{I}}^{I+1} \sigma_{I} + \sum_{p=1}^{P} c_{p}^{I+1} \phi_{p}^{I+1}, \qquad \mathbf{r} \in \Omega_{I+1},$$

$$(16)$$

where the unknowns are the density functions τ_i and σ_i , $1 \le i \le I$, and the proxy strengths $c^i := \{c_n^i\}_{n=1}^P$, $1 \le i \le I+1$.

The ansatz (16) must satisfy the continuity conditions at the interfaces Γ_i , the quasi-periodic conditions, and the radiation conditions. Following a similar procedure as in [30,27], one can substitute the ansatz (16) into (5)–(8) and use the standard jump relations [48, Thm 3.1] to obtain a linear system

$$A\eta + Bc = f, (17)$$

$$C\eta + Qc = 0, (18)$$

$$Z\eta + Vc + Wa = 0, (19)$$

where we will next define the matrices and vectors in the system.

The first two equations (17) and (18), respectively, account for the continuity conditions at the interfaces and the quasi-periodic conditions, where A is an I-by-I block-tridiagonal matrix with the nonzero blocks

$$\begin{aligned}
\{\mathbf{A}_{i,i}\}_{i=1}^{I} &= \begin{bmatrix} \mathbf{I} + (\tilde{D}_{\Gamma_{i}\Gamma_{i}}^{i} - \tilde{D}_{\Gamma_{i}\Gamma_{i}}^{i+1}) & (\tilde{S}_{\Gamma_{i}\Gamma_{i}}^{i} - \tilde{S}_{\Gamma_{i}\Gamma_{i}}^{i+1}) \\ (\tilde{T}_{\Gamma_{i}}^{i} - \tilde{T}_{\Gamma_{i}\Gamma_{i}}^{i+1}) & -\mathbf{I} + (\tilde{D}_{\Gamma_{i}}^{i,*} - \tilde{D}_{\Gamma_{i}\Gamma_{i}}^{i+1,*}) \end{bmatrix}, \\
\{\mathbf{A}_{i,i+1}\}_{i=1}^{I-1} &= \begin{bmatrix} -\tilde{D}_{\Gamma_{i}\Gamma_{i+1}}^{i+1} & -\tilde{S}_{\Gamma_{i}\Gamma_{i+1}}^{i+1} \\ -\tilde{T}_{\Gamma_{i}\Gamma_{i+1}}^{i+1} & -\tilde{D}_{\Gamma_{i}\Gamma_{i+1}}^{i+1,*} \end{bmatrix}, \\
\{\mathbf{A}_{i+1,i}\}_{i=1}^{I-1} &= \begin{bmatrix} \tilde{D}_{\Gamma_{i+1}\Gamma_{i}}^{i+1} & \tilde{S}_{\Gamma_{i+1}\Gamma_{i}}^{i+1} \\ \tilde{T}_{\Gamma_{i+1}\Gamma_{i}}^{i+1} & \tilde{D}_{\Gamma_{i+1}\Gamma_{i}}^{i+1,*} \end{bmatrix}, \end{aligned} \tag{20}$$

B is an I-by-(I + 1) block-bidiagonal matrix with the nonzero blocks

$$\left\{\mathbf{B}_{i,i}\right\}_{i=1}^{I} = \begin{bmatrix} \phi_{1}^{i} \middle|_{\Gamma_{i}} & \dots & \phi_{P}^{i} \middle|_{\Gamma_{i}} \\ \frac{\partial \phi_{1}^{i}}{\partial \mathbf{n}} \middle|_{\Gamma_{i}} & \dots & \frac{\partial \phi_{P}^{i}}{\partial \mathbf{n}} \middle|_{\Gamma_{i}} \end{bmatrix}, \\ \left\{\mathbf{B}_{i,i+1}\right\}_{i=1}^{I} = \begin{bmatrix} -\phi_{1}^{i+1} \middle|_{\Gamma_{i}} & \dots & -\phi_{P}^{i+1} \middle|_{\Gamma_{i}} \\ -\frac{\partial \phi_{1}^{i+1}}{\partial \mathbf{n}} \middle|_{\Gamma_{i}} & \dots & -\frac{\partial \phi_{P}^{i+1}}{\partial \mathbf{n}} \middle|_{\Gamma_{i}} \end{bmatrix},$$

$$(21)$$

C is an (I + 1)-by-I block-bidiagonal matrix with the nonzero blocks

$$\{\mathbf{C}_{i,i}\}_{i=1}^{I} = \sum_{\substack{-1 \leq i \leq 1\\ \mathbf{d}_{\mathbf{x}} = d(1,1,0)\\ \mathbf{d}_{\mathbf{y}} = d(1,1,0)}} \begin{bmatrix} \alpha_{\mathbf{x}}^{-1} \mathcal{D}_{R_{i}+\mathbf{d}_{\mathbf{x}}\Gamma_{i}}^{i} - \alpha_{\mathbf{x}}^{2} \mathcal{D}_{L_{i}-\mathbf{d}_{\mathbf{x}}\Gamma_{i}}^{i} & \alpha_{\mathbf{x}}^{-1} \mathcal{S}_{R_{i}+\mathbf{d}_{\mathbf{x}}\Gamma_{i}}^{i} - \alpha_{\mathbf{x}}^{2} \mathcal{S}_{L_{i}-\mathbf{d}_{\mathbf{x}}\Gamma_{i}}^{i}\\ \alpha_{\mathbf{x}}^{-1} \mathcal{T}_{R_{i}+\mathbf{d}_{\mathbf{x}}\Gamma_{i}}^{i} - \alpha_{\mathbf{x}}^{2} \mathcal{T}_{L_{i}-\mathbf{d}_{\mathbf{x}}\Gamma_{i}}^{i} & \alpha_{\mathbf{x}}^{-1} \mathcal{D}_{R_{i}+\mathbf{d}_{\mathbf{x}}\Gamma_{i}}^{i} - \alpha_{\mathbf{x}}^{2} \mathcal{D}_{L_{i}-\mathbf{d}_{\mathbf{x}}\Gamma_{i}}^{i}\\ \alpha_{\mathbf{y}}^{-1} \mathcal{D}_{B_{i}+\mathbf{d}_{\mathbf{y}}\Gamma_{i}}^{i} - \alpha_{\mathbf{y}}^{2} \mathcal{D}_{F_{i}-\mathbf{d}_{\mathbf{y}}\Gamma_{i}}^{i} & \alpha_{\mathbf{y}}^{-1} \mathcal{D}_{B_{i}+\mathbf{d}_{\mathbf{y}}\Gamma_{i}}^{i} - \alpha_{\mathbf{y}}^{2} \mathcal{D}_{F_{i}-\mathbf{d}_{\mathbf{y}}\Gamma_{i}}^{i}\\ \alpha_{\mathbf{y}}^{-1} \mathcal{D}_{B_{i}+\mathbf{d}_{\mathbf{y}}\Gamma_{i}}^{i} - \alpha_{\mathbf{y}}^{2} \mathcal{D}_{F_{i}-\mathbf{d}_{\mathbf{y}}\Gamma_{i}}^{i} & \alpha_{\mathbf{y}}^{-1} \mathcal{D}_{B_{i}+\mathbf{d}_{\mathbf{y}}\Gamma_{i}}^{i} - \alpha_{\mathbf{y}}^{2} \mathcal{D}_{F_{i}-\mathbf{d}_{\mathbf{y}}\Gamma_{i}}^{i}\\ \alpha_{\mathbf{y}}^{-1} \mathcal{D}_{B_{i}+\mathbf{d}_{\mathbf{y}}\Gamma_{i}}^{i} - \alpha_{\mathbf{y}}^{2} \mathcal{D}_{F_{i}-\mathbf{d}_{\mathbf{y}}\Gamma_{i}}^{i} & \alpha_{\mathbf{y}}^{-1} \mathcal{D}_{B_{i}+\mathbf{d}_{\mathbf{y}}\Gamma_{i}}^{i} - \alpha_{\mathbf{y}}^{2} \mathcal{D}_{F_{i}-\mathbf{d}_{\mathbf{y}}\Gamma_{i}}^{i}\\ \alpha_{\mathbf{y}}^{-1} \mathcal{D}_{B_{i+1}+\mathbf{d}_{\mathbf{y}}\Gamma_{i}}^{i} - \alpha_{\mathbf{y}}^{2} \mathcal{D}_{F_{i+1}-\mathbf{d}_{\mathbf{y}}\Gamma_{i}}^{i} & \alpha_{\mathbf{y}}^{-1} \mathcal{D}_{B_{i+1}+\mathbf{d}_{\mathbf{y}}\Gamma_{i}}^{i} - \alpha_{\mathbf{y}}^{2} \mathcal{D}_{F_{i+1}-\mathbf{d}_{\mathbf{y}}\Gamma_{i}}^{i}\\ \alpha_{\mathbf{y}}^{-1} \mathcal{D}_{B_{i+1}+\mathbf{d}_{\mathbf{y}}\Gamma_{i}}^{i} - \alpha_{\mathbf{y}}^{2} \mathcal{D}_{F_{i+1}-\mathbf{d}_{\mathbf{y}}\Gamma_{i}}^{i} & \alpha_{\mathbf{y}}^{-1} \mathcal{D}_{B_{i+1}+\mathbf{d}_{\mathbf{y}}\Gamma_{i}}^{i} - \alpha_{\mathbf{y}}^{2} \mathcal{D}_{F_{i+1}-\mathbf{d}_{\mathbf{y}}\Gamma_{i}}^{i}\\ \alpha_{\mathbf{y}}^{-1} \mathcal{D}_{B_{i+1}+\mathbf{d}_{\mathbf{y}}\Gamma_{i}}^{i} - \alpha_{\mathbf{y}}^{2} \mathcal{D}_{F_{i+1}-\mathbf{d}_{\mathbf{y}}\Gamma_{i}}^{i} & \alpha_{\mathbf{y}}^{-1} \mathcal{D}_{B_{i+1}+\mathbf{d}_{\mathbf{y}}\Gamma_{i}}^{i} - \alpha_{\mathbf{y}}^{2} \mathcal{D}_{F_{i+1}-\mathbf{d}_{\mathbf{y}}\Gamma_{i}}^{i}\\ \alpha_{\mathbf{y}}^{-1} \mathcal{D}_{B_{i+1}+\mathbf{d}_{\mathbf{y}}\Gamma_{i}}^{i} - \alpha_{\mathbf{y}}^{2} \mathcal{D}_{F_{i+1}-\mathbf{d}_{\mathbf{y}}\Gamma_{i}}^{i} & \alpha_{\mathbf{y}}^{-1} \mathcal{D}_{B_{i+1}+\mathbf{d}_{\mathbf{y}}\Gamma_{i}}^{i} - \alpha_{\mathbf{y}}^{2} \mathcal{D}_{F_{i+1}-\mathbf{d}_{\mathbf{y}}\Gamma_{i}}^{i}\\ \alpha_{\mathbf{y}}^{-1} \mathcal{D}_{\mathbf{y}}^{i+1} \mathcal{D}_{\mathbf{y}}^{i} - \alpha_{\mathbf{y}}^{2} \mathcal{D}_{\mathbf{y}}^{i+1} \mathcal{D}_{\mathbf{y}}^{i} - \alpha_{\mathbf{y}}^{2} \mathcal{D}_{\mathbf{y}}^{i+1} \mathcal{D}_{\mathbf{y}}^{i}$$

and \mathbf{Q} is an (I+1)-by-(I+1) block-diagonal matrix with the nonzero blocks

$$\left\{\mathbf{Q}_{i,i}\right\}_{i=1}^{I+1} = \begin{bmatrix} \phi_{1}^{i} \Big|_{R_{i}} - \alpha_{x} \phi_{1}^{i} \Big|_{L_{i}} & \dots & \phi_{P}^{i} \Big|_{R_{i}} - \alpha_{x} \phi_{P}^{i} \Big|_{L_{i}} \\ \frac{\partial \phi_{1}^{i}}{\partial n} \Big|_{R_{i}} - \alpha_{x} \frac{\partial \phi_{1}^{i}}{\partial n} \Big|_{L_{i}} & \dots & \frac{\partial \phi_{P}^{i}}{\partial n} \Big|_{R_{i}} - \alpha_{x} \frac{\partial \phi_{P}^{i}}{\partial n} \Big|_{L_{i}} \\ \phi_{1}^{i} \Big|_{B_{i}} - \alpha_{y} \phi_{1}^{i} \Big|_{F_{i}} & \dots & \phi_{P}^{i} \Big|_{B_{i}} - \alpha_{y} \phi_{P}^{i} \Big|_{F_{i}} \\ \frac{\partial \phi_{1}^{i}}{\partial n} \Big|_{B_{i}} - \alpha_{y} \frac{\partial \phi_{1}^{i}}{\partial n} \Big|_{F_{i}} & \dots & \frac{\partial \phi_{P}^{i}}{\partial n} \Big|_{B_{i}} - \alpha_{y} \frac{\partial \phi_{P}^{i}}{\partial n} \Big|_{F_{i}} \end{bmatrix}. \tag{23}$$

The corresponding vectors in Eqs. (17) and (18), including the densities η on the interfaces, the proxy source strengths c on the proxy spheres, and the right-hand side functions f, are given by

$$\eta = \begin{bmatrix} \eta_1 & \dots & \eta_I \end{bmatrix}^T, \text{ where } \eta_i := \begin{bmatrix} \tau_i \\ \sigma_i \end{bmatrix},
\mathbf{c} = \begin{bmatrix} c^1 & \dots & c^{I+1} \end{bmatrix}^T, \mathbf{f} = \begin{bmatrix} -u^{\text{inc}} |_{\Gamma_1} & -\frac{\partial u^{\text{inc}}}{\partial \mathbf{n}} |_{\Gamma_1} & 0 & \dots & 0 \end{bmatrix}^T.$$
(24)

Equation (19) accounts for the radiation conditions at the artificial interfaces U and D. The matrix \mathbf{Z} is a 2-by-I block-sparse matrix, given by

$$\mathbf{Z} = \begin{bmatrix} \mathbf{Z}_U & \mathbf{0} & \dots & \mathbf{0} \\ \mathbf{0} & \dots & \mathbf{0} & \mathbf{Z}_D \end{bmatrix}, \tag{25}$$

where

$$\mathbf{Z}_{U} = \begin{bmatrix} \tilde{D}_{U,\Gamma_{1}}^{1} & \tilde{S}_{U,\Gamma_{1}}^{1} \\ \tilde{T}_{U,\Gamma_{1}}^{1} & \tilde{D}_{U,\Gamma_{1}}^{1,*} \end{bmatrix}, \mathbf{Z}_{D} = \begin{bmatrix} D_{D,\Gamma_{1}}^{I+1} & S_{D,\Gamma_{1}}^{I+1} \\ D_{D,\Gamma_{1}}^{I+1} & D_{D,\Gamma_{1}}^{I+1,*} \end{bmatrix},$$
(26)

and the matrix V a 2-by-(I+1) block-sparse matrix, given by

$$\mathbf{V} = \begin{bmatrix} \mathbf{V}_U & \mathbf{0} & \dots & \mathbf{0} \\ \mathbf{0} & \dots & \mathbf{0} & \mathbf{V}_D \end{bmatrix},\tag{27}$$

where

$$\mathbf{V}_{U} = \begin{bmatrix} \phi_{1}^{1} |_{U} & \cdots & \phi_{P}^{1} |_{U} \\ \frac{\partial \phi_{1}^{1}}{\partial n} |_{U} & \cdots & \frac{\partial \phi_{P}^{1}}{\partial n} |_{U} \end{bmatrix}, \mathbf{V}_{D} = \begin{bmatrix} \phi_{1}^{I+1} |_{D} & \cdots & \phi_{P}^{I+1} |_{D} \\ \frac{\partial \phi_{1}^{I+1}}{\partial n} |_{D} & \cdots & \frac{\partial \phi_{P}^{I+1}}{\partial n} |_{D} \end{bmatrix}, \tag{28}$$

and W is a 2-by-2 block-diagonal matrix, in which the (1,1)-component \mathbf{W}_U and the (2,2)-component \mathbf{W}_D are given by

$$\mathbf{W}_{U} = \begin{bmatrix} -e^{i(\kappa_{X}^{m} \mathbf{x} + \kappa_{y}^{n} \mathbf{y})} \Big|_{U} \\ -ik_{\mathbf{u}}^{(m,n)} e^{i(\kappa_{X}^{m} \mathbf{x} + \kappa_{y}^{n} \mathbf{y})} \Big|_{U} \end{bmatrix}, \mathbf{W}_{D} = \begin{bmatrix} -e^{i(\kappa_{X}^{m} \mathbf{x} + \kappa_{y}^{n} \mathbf{y})} \Big|_{D} \\ ik_{d}^{(m,n)} e^{i(\kappa_{X}^{m} \mathbf{x} + \kappa_{y}^{n} \mathbf{y})} \Big|_{D} \end{bmatrix},$$
(29)

where m, n = -K, -K + 1, ..., K - 1, K. The corresponding vector $\mathbf{a} = [\mathbf{a}^{\mathrm{u}} \ \mathbf{a}^{\mathrm{d}}]^T$ contains the Rayleigh-Block coefficients such that $\mathbf{a}^{\mathrm{u}} = [a_{mn}^{\mathrm{u}}]$ and $\mathbf{a}^{\mathrm{d}} = [a_{mn}^{\mathrm{d}}], m, n = -K, -K + 1, ..., K - 1, K$.

Remark 1. Note that in Eq. (22), the operators in the C matrix are the ordinary layer potential operators (ones without "tilde") where the source and target geometries for each operator are separated by a distance of d. This is a consequence of the translational symmetry of the integral operators which has led to the cancellations of all the near interactions in the periodized operators (ones with "tilde"). As a result, all of the interactions represented by C are distant and smooth, which can be discretized using ordinary smooth quadrature rules. The same simplification technique has been used in [27,51,53].

2.1. Discretization of functions and operators

To accurately solve the system (17)-(19), we describe high-order collocation methods for the discretization of the integral operators in A. C. Z and the functions in the rest of the matrix blocks.

We choose collocation points on the interfaces and the walls as follows. On each side wall W, where W is one of R_i , L_i , R_i , and R_i , for $i=1,\ldots,I+1$, we sample M_w points $\{\mathbf{x}_m^W\}_{m=1}^{M_w}$ that correspond to a 2-D tensor product of 1-D quadrature nodes. For the top and bottom walls U and D, we use M equally-spaced nodes (associated with the double Trapezoidal rule) $\{\mathbf{x}_m^U\}_{m=1}^M$ on U and $\{\mathbf{x}_m^D\}_{m=1}^M$ on U. For the interfaces Γ_i which are smooth and doubly periodic, we assume the parameterizations R_i on the rectangle $[0,1]^2$ are given by

$$\Gamma_i = \{ \mathbf{r} = (x, y, z) \mid z = g_i(x, y), (x, y) \in [0, 1]^2 \}.$$
(30)

Fixing a set of N equally-spaced nodes $\{(x_n,y_n)\}_{n=1}^N\subset [0,1]^2$ associated with the double Trapezoidal rule, we can then sample Γ_i at N points $\{\mathbf{x}_n^i=(x_n,y_n,g_i(x_n,y_n))\}_{n=1}^N$; let $\{w_n^i\}_{n=1}^N$ be the associated quadrature weights such that

$$\int_{\Gamma_i} f(\mathbf{r}) \, \mathrm{d}S_{\mathbf{r}} \approx \sum_{n=1}^N f(\mathbf{x}_n^i) w_n^i \tag{31}$$

holds to high accuracy for any given smooth periodic function f on Γ_i .

The discretization of the matrix blocks in the system (17)-(19) becomes straightforward with the collocation points and the quadrature above (except for the diagonal blocks of A, which we will address shortly). For example, in the $\mathbf{Q}_{i,i}$ block in (23), an entry $\phi_p^i \Big|_{R_i} - \alpha_x \phi_p^i \Big|_{L_i}$ in the first row is replaced by an $M_w \times P$ matrix

$$\left(\phi_n^i(\mathbf{x}_m^{R_i}) - \alpha_x \phi_n^i(\mathbf{x}_m^{L_i})\right), \quad m = 1, \dots, M_w, p = 1, \dots, P.$$

All the entries in **B**, **Q**, **V**, and **W** can be discretized similarly. On the other hand, the operators in **A**, **C**, **Z** (except for the diagonal blocks of **A**) can be discretized using the smooth quadrature (31). For example in the $C_{i,i}$ block in (22), an operator $\alpha_x^{-1} S_{R_i + \mathbf{d}_x, \Gamma_i}^i - \alpha_x^2 S_{L_i - \mathbf{d}_x, \Gamma_i}^i$ can be discretized as an $M_w \times N$ matrix

$$\left(\alpha_x^{-1}G^i(\mathbf{x}_m^{R_i}+\mathbf{d}_x,\mathbf{x}_n^i)w_n^i-\alpha_x^2G^i(\mathbf{x}_m^{L_i}-\mathbf{d}_x,\mathbf{x}_n^i)w_n^i\right),$$

where $m = 1, ..., M_w$, n = 1, ..., N. We now consider the discretization of the diagonal blocks $\mathbf{A}_{i,i}$ in (20). These blocks involve interactions from Γ_i to itself, where the involved integrals become singular, so the smooth quadrature ceases to be accurate. We will focus on discretizing the entries involving the single-layer operator \tilde{S} ; other self-interactions involving the operators \tilde{D}, \tilde{D}^* , and \tilde{T} can then be discretized similarly. Consider $\tilde{S}_{\Gamma_1,\Gamma_1}^1 - \tilde{S}_{\Gamma_1,\Gamma_1}^2$ in the $\mathbf{A}_{1,1}$ block, the associated integral operator is

$$\left((\tilde{S}_{\Gamma_{1},\Gamma_{1}}^{1} - \tilde{S}_{\Gamma_{1},\Gamma_{1}}^{2}) \sigma \right) (\mathbf{r}) = \sum_{\substack{-1 \le l_{x}, l_{y} \le 1 \\ \mathbf{d} = d(l_{x}, l_{y}, 0)}} a_{x}^{l_{x}} \alpha_{y}^{l_{y}} \int_{\Gamma_{1}} \left(G^{1}(\mathbf{r}, \mathbf{r}' + \mathbf{d}) - G^{2}(\mathbf{r}, \mathbf{r}' + \mathbf{d}) \right) \sigma(\mathbf{r}') \, \mathrm{d}S_{\mathbf{r}'}, \, \mathbf{r} \in \Gamma_{1},$$

$$(32)$$

which consists of contributions from $\Gamma_1 + \mathbf{d}$ to Γ_1 . When $\mathbf{d} \neq \mathbf{0}$, one can still discretize (32) using the smooth quadrature (31) with nodes $\{\mathbf{x}_n^1 + \mathbf{d}\}_{n=1}^N$ and weights $\{w_n^1\}_{n=1}^N$. When $\mathbf{d} = \mathbf{0}$, applying the smooth quadrature will result in a matrix

$$\left(S_{\Gamma_{1},\Gamma_{1}}^{1} - S_{\Gamma_{1},\Gamma_{1}}^{2}\right)_{m,n} = \left(G^{1}(\mathbf{x}_{m}^{1}, \mathbf{x}_{n}^{1}) - G^{2}(\mathbf{x}_{m}^{1}, \mathbf{x}_{n}^{1})\right) w_{n}^{1}, \quad m, n = 1, \dots, N$$
(33)

whose diagonal entries are infinite; zeroing out the diagonal entries (i.e., using the "punctured Trapezoidal rule") will allow the discretization to converge as $N \to \infty$, but only very slowly. We next describe a new quadrature that makes corrections near the diagonal of (33) to obtain a high-order discretization.

2.2. Special quadrature for self interaction

We describe a specialized quadrature for (32) which modifies the entries of (33). This quadrature is based on the error-corrected Trapezoidal quadrature method [45], which is a recent generalization of [44] that achieves high-order accuracies. For a fixed target point $\mathbf{r}_0 := \mathbf{x}_m^1 \in \Gamma_1$ (where m is fixed), consider the integral

$$I = \int_{\Gamma_1} \left(G^1(\mathbf{r}_0, \mathbf{r}) - G^2(\mathbf{r}_0, \mathbf{r}) \right) \sigma(\mathbf{r}) \, \mathrm{d}S_{\mathbf{r}}$$
(34)

and its boundary-corrected, punctured Trapezoidal rule approximation

$$Q_h = \sum_{\substack{n=1\\n\neq m}}^{N} \left(G^1(\mathbf{x}_m^1, \mathbf{x}_n^1) - G^2(\mathbf{x}_m^1, \mathbf{x}_n^1) \right) w_n^1 \sigma(\mathbf{x}_n^1) + C_h, \tag{35}$$

where h is the grid spacing, and where the boundary correction C_h is a linear combination of the values and derivatives of the integrand in (34); the coefficients of the linear combination appears in the two-dimensional Euler-Maclaurin formula (see, for example, [54, Theorem 2.6]) and do not depend on the integrand. The exact form of C_h is unimportant for our purpose, because the surface Γ_1 is periodic thus the boundary errors will vanish. To analyze the error of $I-Q_h$, we only need to assume that C_h is a sufficiently high-order boundary correction so that the dominant error always comes from the singularity of the integrand.

Lemma 1. The error of the Trapezoidal rule approximation of (34), $E_h := I - Q_h$, has an asymptotic expansion

$$E_h \sim c_1 h^3 + c_2 h^5 + \dots = \sum_{p=1}^{\infty} c_p h^{2p+1}, \quad \text{as } h \to 0,$$
 (36)

where the coefficients $c_1, c_2,...$ only depend on the following information at the target point \mathbf{r}_0 : the derivatives of the parameterization of the surface Γ_1 at \mathbf{r}_0 , and the value and derivatives of a smooth function $\varphi(\mathbf{r})$ at \mathbf{r}_0 , where $\varphi(\mathbf{r})$ can be explicitly constructed from the integrand of (34).

Proof. Let $r := |\mathbf{r}_0 - \mathbf{r}|$, then using the definition (10) and the parameterization, the integral (34) can be rewritten as

$$I = \int_{0}^{1} \int_{0}^{1} \left(r \psi_{c}(r) + i \psi_{s}(r) \right) \sigma(\mathbf{r}) J(\mathbf{r}) dx dy$$

$$= \int_{0}^{1} \int_{0}^{1} r \psi_{c}(r) \sigma(\mathbf{r}) J(\mathbf{r}) dx dy + i \int_{0}^{1} \int_{0}^{1} \psi_{s}(r) \sigma(\mathbf{r}) J(\mathbf{r}) dx dy$$

$$:= I_{1} + i I_{2}$$

$$(37)$$

where $\mathbf{r} = \mathbf{r}(x, y)$ is the parameterization (30) for Γ_1 , where $J(\mathbf{r})$ is the Jacobian, and where

$$\psi_c(r) := \frac{\cos(k_1 r) - \cos(k_2 r)}{r^2}$$
 and $\psi_s(r) := \frac{\sin(k_1 r) - \sin(k_2 r)}{r}$

are smooth functions of $r^2 = |\mathbf{r}_0 - \mathbf{r}|^2$, thus are also smooth functions of \mathbf{r} on Γ_1 . The Trapezoidal rule approximation $Q_h = Q_{h,1} + iQ_{h,2}$ where $Q_{h,1}$ and $Q_{h,2}$ are the approximation of the integrals I_1 and I_2 , respectively. The imaginary component I_2 is smooth thus the approximation $Q_{h,2}$ is high-order accurate, so the error $E_h \sim I_1 - Q_{h,1}$. The integrand of I_1 can be written as $r \varphi(\mathbf{r})$, where

$$\varphi(\mathbf{r}) := \psi_r(r)\sigma(\mathbf{r})J(\mathbf{r}) \tag{38}$$

is a smooth function of $\mathbf{r}(x, y)$. Following [45, Section 3.1], the integrand of I_1 has the following expansion at $\mathbf{r}_0 = \mathbf{r}(x_0, y_0)$

$$r\,\varphi(\mathbf{r}) \sim \sum_{m=0}^{\infty} \sum_{\substack{n=3m\\l_1,l_2 \geq 0}}^{\infty} \sum_{\substack{l_1,l_2 \geq 0\\l_1,l_2 = n}}^{\infty} \alpha_{l_1,l_2}^{m,n} \frac{\hat{\mathbf{x}}^{l_1} \hat{\mathbf{y}}^{l_2}}{\mathcal{F}(\hat{\mathbf{x}}, \hat{\mathbf{y}})^{m-1/2}} \tag{39}$$

where $\hat{x} = x - x_0$ and $\hat{y} = y - y_0$, where the coefficients $\alpha_{l_1, l_2}^{m,n}$ depend on the value and derivatives of φ and $\mathbf{r}(x, y)$ at (x_0, y_0) , and where $\mathcal{F}(x, y)$ is the first fundamental form of Γ_1 at \mathbf{r}_0 defined as

$$F(\hat{x}, \hat{y}) = E\hat{x}^2 + 2F\hat{x}\hat{y} + G\hat{y}^2,$$
 (40)

where

$$E = |\mathbf{r}_{\mathbf{x}}(x_0, y_0)|^2, \ F = \mathbf{r}_{\mathbf{x}}(x_0, y_0) \cdot \mathbf{r}_{\mathbf{v}}(x_0, y_0), \ G = |\mathbf{r}_{\mathbf{v}}(x_0, y_0)|^2.$$

$$(41)$$

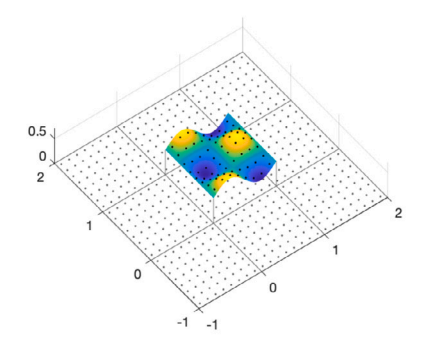
Then applying the generalized Euler-Maclaurin formula [45, Theorem 3.2], we have

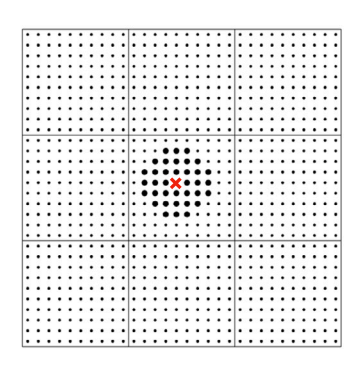
$$E_h \sim I_1 - Q_{h,1} \sim \sum_{m=0}^{\infty} \sum_{\substack{n=3m\\ n \text{ even } l_1, l_1 = n}}^{\infty} \sum_{l_1, l_2 \ge 0}^{\infty} -\alpha_{l_1, l_2}^{m, n} C_{l_1, l_2}^{m} [E, F, G] h^{n-2m+3}$$

$$(42)$$

where $C_{l_1,l_2}^m[E,F,G]$ are coefficients that only depend on E,F,G and can be computed based on [45, Theorem 3.3]. To finish the proof, the equation (42) can be rearranged into the form (36) by grouping the terms by the powers of h. \square

A high-order corrected Trapezoidal rule for the integral operator (34) can then be constructed by adding a sufficient number of terms in the error expansion (36). However, a direct computation of (36) requires approximating the higher derivatives of φ and $\mathbf{r}(x,y)$. To avoid computing these higher derivatives, the *moment-fitting procedure* from [45, Section 3.2] is used to fit the error (36) on a local stencil around the target point \mathbf{r}_0 , this procedure only requires evaluating $\varphi(\mathbf{r})$, $\mathbf{r}(x,y)$ and the first fundamental form $\mathcal{F}(\hat{x},\hat{y})$ on the stencil. Fig. 2 shows the stencil for a 5th order correction; note that when the stencil extends outside the central domain, the corresponding weights should be constructed with appropriate phased contribution involving the Bloch phases α_x and α_y . We refer to [45] for more details on higher order discretization.





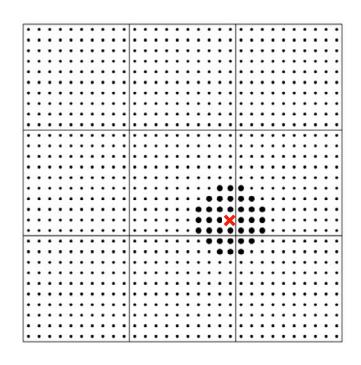


Fig. 2. Left: A doubly periodic surface with period d = 1 and parameterized over $[0, 1]^2$, sampled with equally-spaced nodes $\{x_n^i\}_{n=1}^N$. The nodes in the parameter space, $\{(x_n, y_n)\}_{n=1}^N \subset [0, 1]^2$ in the xy-plane, together with their copies in the 8 nearest neighbors, are shown in all three panels. Middle: local error-correction stencil (thick dots) around a target point (red cross) in the middle of the domain. Right: error-correction stencil around a target point near the edge of the domain; note that the stencil extends outside the domain to the near periodic copies. (For interpretation of the colors in the figure(s), the reader is referred to the web version of this article.)

3. Rearrangement of equations, block elimination, and fast solver

The system (17)-(19) is sparse and can be transformed into a block-tridiagonal system as follows. First, rearrange the rows and columns of (17)-(19) to form the block 2×2 system

$$\begin{bmatrix} \mathbf{A} & \tilde{\mathbf{B}} \\ \tilde{\mathbf{C}} & \tilde{\mathbf{Q}} \end{bmatrix} \begin{bmatrix} \eta \\ \tilde{\mathbf{c}} \end{bmatrix} = \begin{bmatrix} \mathbf{f} \\ \mathbf{0} \end{bmatrix}, \tag{43}$$

where one combines c_1 and a^u , and respectively c_{I+1} and a^d , to form

$$\tilde{\mathbf{c}}_{1} = \begin{bmatrix} \mathbf{c}_{1} \\ \mathbf{a}^{\mathrm{u}} \end{bmatrix}, \quad \tilde{\mathbf{c}}_{I+1} = \begin{bmatrix} \mathbf{c}_{I+1} \\ \mathbf{a}^{\mathrm{d}} \end{bmatrix}, \quad \tilde{\mathbf{c}} = \begin{bmatrix} \tilde{\mathbf{c}}_{1} & \mathbf{c}_{2} & \dots & \mathbf{c}_{I} & \tilde{\mathbf{c}}_{I+1} \end{bmatrix}^{T}$$

$$(44)$$

and, accordingly, $\tilde{\mathbf{Q}}$ is formed by replacing the (1,1)-block and the (I+1,I+1)-block of \mathbf{Q} with

$$\tilde{\mathbf{Q}}_{1,1} = \begin{bmatrix} \mathbf{Q}_{1,1} & \mathbf{0} \\ \mathbf{V}_{II} & \mathbf{W}_{II} \end{bmatrix}, \quad \tilde{\mathbf{Q}}_{I+1,I+1} = \begin{bmatrix} \mathbf{Q}_{I+1,I+1} & \mathbf{0} \\ \mathbf{V}_{D} & \mathbf{W}_{D} \end{bmatrix}. \tag{45}$$

Likewise, $\tilde{\mathbf{B}}$ and $\tilde{\mathbf{C}}$ are formed, respectively, by replacing the (1,1)-block and the (I,I+1)-block of \mathbf{B} , and replacing the (1,1)-block and the (I+1,I)-block of \mathbf{C} , with

$$\tilde{\mathbf{B}}_{1,1} = \begin{bmatrix} \mathbf{B}_{1,1} & \mathbf{0} \end{bmatrix}, \quad \tilde{\mathbf{B}}_{I,I+1} = \begin{bmatrix} \mathbf{B}_{I,I+1} & \mathbf{0} \end{bmatrix},
\tilde{\mathbf{C}}_{1,1} = \begin{bmatrix} \mathbf{C}_{1,1} \\ \mathbf{Z}_{U} \end{bmatrix}, \quad \tilde{\mathbf{C}}_{I+1,I} = \begin{bmatrix} \mathbf{C}_{I+1,I} \\ \mathbf{Z}_{D} \end{bmatrix}.$$
(46)

Next, eliminate the unknowns \tilde{c} to reduce the system (43) into block tridiagonal form

$$\tilde{\mathbf{A}}\boldsymbol{\eta} = \mathbf{f},\tag{47}$$

where $\tilde{\mathbf{A}}$ is an $I \times I$ block tridiagonal matrix with the nonzero blocks

$$\tilde{\mathbf{A}}_{1,1} = \mathbf{A}_{1,1} - \tilde{\mathbf{B}}_{1,1} \tilde{\mathbf{Q}}_{1,1}^{\dagger} \tilde{\mathbf{C}}_{1,1} - \mathbf{B}_{1,2} \mathbf{Q}_{2,2}^{\dagger} \mathbf{C}_{2,1}, \tag{48}$$

$$\tilde{\mathbf{A}}_{i,i} = \mathbf{A}_{i,i} - \mathbf{B}_{i,i} \mathbf{Q}_{i,i}^{\dagger} \mathbf{C}_{i,i} - \mathbf{B}_{i,i+1} \mathbf{Q}_{i+1,i+1}^{\dagger} \mathbf{C}_{i+1,i}, \quad i = 2, 3, \dots, I - 1,$$
(49)

$$\tilde{\mathbf{A}}_{I,I} = \mathbf{A}_{I,I} - \tilde{\mathbf{B}}_{I,I} \tilde{\mathbf{Q}}_{I,I}^{\dagger} \tilde{\mathbf{C}}_{I,I} - \mathbf{B}_{I,I+1} \mathbf{Q}_{I+1,I+1}^{\dagger} \mathbf{C}_{I+1,1},$$
(50)

$$\tilde{\mathbf{A}}_{i,i+1} = \mathbf{A}_{i,i+1} - \mathbf{B}_{i,i+1} \mathbf{Q}_{i+1,i+1}^{\dagger} \mathbf{C}_{i+1,i+1}, \qquad i = 1, 2, 3, \dots, I - 1,$$
(51)

$$\tilde{\mathbf{A}}_{i+1,i} = \mathbf{A}_{i+1,i} - \mathbf{B}_{i+1,i+1} \mathbf{Q}_{i+1,i+1}^{\dagger} \mathbf{C}_{i+1,i}, \qquad i = 1, 2, 3, \dots, I - 1,$$
(52)

where † denotes the pseudo inverse of a rectangular matrix. In practice, the pseudo-inverses $\mathbf{Q}_{i,i}^{\dagger}$ are not computed explicitly; instead, an equation such as $\mathbf{Q}_{i,i}\mathbf{X}=\mathbf{C}_{i,i}$ is solved with a standard backward-stable direct dense solver such as the "mldivide" command in MATLAB. The system (47) can be solved efficiently using the block sparse LU factorization (i.e., block Thomas algorithm) [55, Sec.4.5.1] in $O(N^3I)$ operations, assuming the number of unknowns associated with each interface is O(N). The algorithm proceeds by first initializing $\mathbf{f}_1'=\mathbf{f}_1$ and $\tilde{\mathbf{A}}_{1,1}'=\tilde{\mathbf{A}}_{1,1}$, then a forward sweep for i=2 to I,

$$\begin{split} \tilde{\mathbf{A}}_{i,i}' &= \tilde{\mathbf{A}}_{i,i} - \tilde{\mathbf{A}}_{i,i-1} (\tilde{\mathbf{A}}_{i-1,i-1}')^{-1} \tilde{\mathbf{A}}_{i-1,i}, \\ \mathbf{f}_i' &= \mathbf{f}_i - \tilde{\mathbf{A}}_{i,i-1} (\tilde{\mathbf{A}}_{i-1,i-1}')^{-1} \mathbf{f}_{i-1}', \end{split}$$

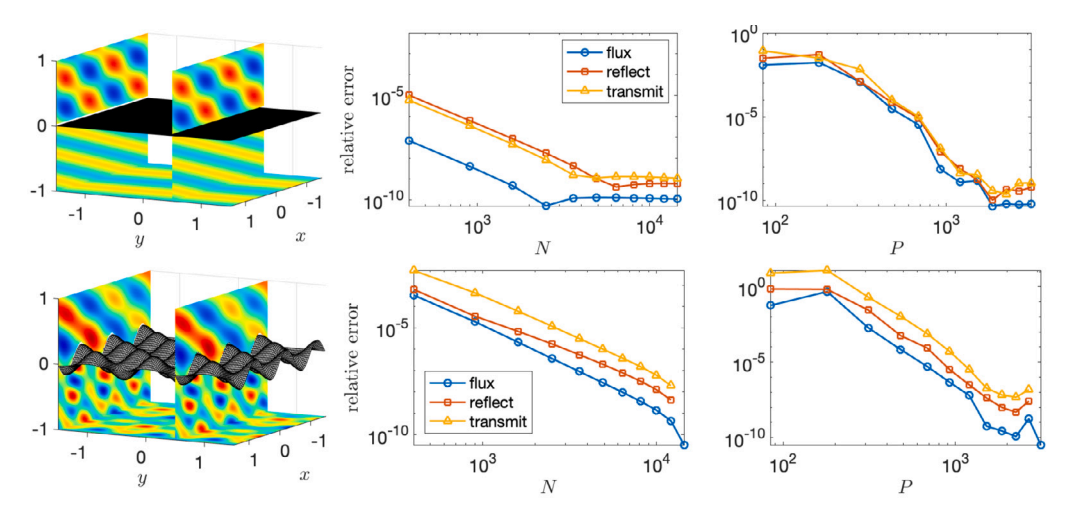


Fig. 3. Two-layered media transmission problem with wavenumbers $k_1 = 8$ and $k_2 = 16$. The incident angle is $\phi^{inc} = \frac{5\pi}{6}$ with $\phi^{inc} = 0$. Results with a flat interface are on the top row, and with a corrugated interface on the bottom row. Left panels: Total field. Middle panels: relative error of the reflected wave (at the point (-0.25, -0.25, 0.25)) and of the transmitted wave (at the point (-0.25, -0.25, -0.25)) and the flux error against N, the number of points per interface. Right panels: convergence and flux error against P, the number of proxy points per layer.

followed by solving $\tilde{\mathbf{A}}_{I,I}' \eta_I = \mathbf{f}_I'$ for η_I , and then a backward sweep for i = I - 1 down to 1 to solve for each η_i ,

$$\boldsymbol{\eta}_i = (\tilde{\mathbf{A}}'_{i,i})^{-1}(\mathbf{f}'_i - \tilde{\mathbf{A}}_{i,i+1}\boldsymbol{\eta}_{i+1}).$$

Once the densities η_i are obtained, the modified proxy strengths $\tilde{\mathbf{c}}_i$ can be recovered by

$$\tilde{\mathbf{c}}_1 = -\tilde{\mathbf{Q}}_{1,1}^{\dagger} \tilde{\mathbf{C}}_{1,1} \boldsymbol{\eta}_1, \tag{53}$$

$$\mathbf{c}_{i} = -\tilde{\mathbf{Q}}_{i,i}^{\dagger}(\tilde{\mathbf{C}}_{i,i-1}\boldsymbol{\eta}_{i-1} + \tilde{\mathbf{C}}_{i,i}\boldsymbol{\eta}_{i}), \qquad i = 2, 3, \dots, I,$$
(54)

$$\tilde{\mathbf{c}}_{I+1} = -\tilde{\mathbf{Q}}_{I+1}^{\dagger} \tilde{\mathbf{C}}_{I+1,I} \eta_{I}. \tag{55}$$

Then substituting the densities η_i and proxy strengths \mathbf{c}_i into the ansatz (16) gives the scattered field at any locations in any given layer Ω_i .

4. Numerical results

In this section, we present numerical examples of multilayered media scattering using the numerical scheme described in the previous sections. We first investigate the convergence of the solutions and the complexity of the computational time and memory requirements, then we show examples of scattering with many layers. Most computations are performed on a Mac Pro with 3.2 GHz 16-Core Intel Xeon W processors and 192 GB RAM using MATLAB R2022a; the 101-layer example in Fig. 6 is performed on a work-station with 3.1 GHz 36-Core Intel Xeon Gold 6254 processors and 768 GB of RAM. The MATLAB code that accompanies this paper can be found in the GitHub repository https://github.com/bobbielf2/ZetaTrap3D_Unified under the folder multilayermedia. In all examples, the incident wave is the plane wave defined in (1). Points on all the surrounding walls are uniformly distributed. The proxy points for each layer are placed on a sphere of radius 1.5 enclosing the unit cell of the layer. (See Fig. 1(b)-(c).) We note that our algorithm accepts both real and complex wavenumbers k_i . We have chosen real k_i in our examples for the convenience of implementation and for the availability of an independent measure for the accuracy which we describe next.

We use the relative flux error $E_{\rm flux}$ as an independent measure of accuracy, which is defined as

$$E_{\text{flux}} := \left| \frac{\sum_{k_{\text{u}}^{(m,n)} > 0} k_{\text{u}}^{(m,n)} |a_{mn}^{\text{u}}|^2 + \sum_{k_{\text{d}}^{(m,n)} > 0} k_{\text{d}}^{(m,n)} |a_{mn}^{\text{d}}|^2 - k_1 \cos \phi^{\text{inc}}}{k_1 \cos \phi^{\text{inc}}} \right|.$$
 (56)

This measure is based on the conservation of flux (energy) [30].

Convergence of the solutions The first example considers the transmission problem with a two-layered media, where the interface Γ_1 , parameterized by $g_1(x,y) = h \sin(2\pi x) \cos(2\pi y)$, is either flat (h=0) or corrugated (h=0.2). The wavenumbers in the top and bottom layers are $k_1=8$ and $k_2=16$ and the incident angle is $\phi^{\rm inc}=\frac{5\pi}{6}$ and $\theta^{\rm inc}=0$. In Fig. 3, we test the convergence of the scattered field u at the point (-0.25, -0.25, 0.25) in the top layer (i.e. the reflected field) and at the point (-0.25, -0.25, -0.25) in the bottom layer (i.e. the transmitted field), and investigate the relative flux error $E_{\rm flux}$. The convergence against N, the number of points per interface, and against P, the number of proxy points per layer, are shown, where the analytic solution is used as the reference solution in the flat case and the numerical solution with $N=120^2$ and P=3120 is used as the reference solution in the corrugated case. Other

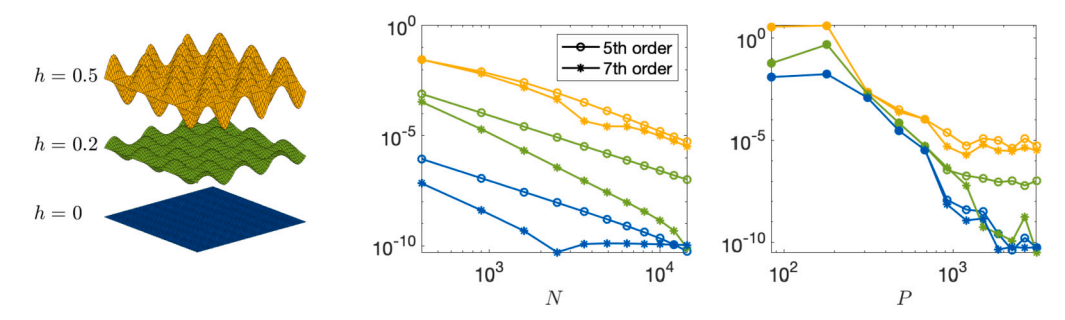


Fig. 4. Investigation of the effects of different levels of roughness of the interface and the order of the quadrature correction on the convergence of the two-layered media problem in Fig. 3. Left panel illustrates the surface $g_1(x,y) = h \sin(2\pi x) \cos(2\pi y)$ for three different values of h. (Note: this is *not* the actual arrangement of interfaces.) Convergence of flux error against N (middle panel) and against P (right panel) are shown for the cases h = 0 (blue), h = 0.2 (green) and h = 0.5 (yellow), with quadrature corrections of 5th order (circles) and of 7th order (asterisks) with respect to the grid spacing. All other parameters are the same as in Fig. 3.

Table 1 Time (in seconds) and memory (in gigabytes) requirements for multilayered media scattering, where I is the number of interfaces

I	1	2	3	4	5	10	20	30
T_{pre} (s)	4	8	13	17	21	42	84	125
$T_{\rm fill}$ (s)	23	65	107	149	191	390	797	1203
T_{solve} (s)	16	43	73	103	133	280	575	875
$M_{\rm fill}$ (GB)	2.0	5.2	8.4	11.7	14.9	31.0	63.3	95.6
$E_{ m flux}$	8.5e-08	3.1e-06	2.9e-06	4.8e-06	4.6e-06	4.9e-06	4.9e-06	4.9e-06

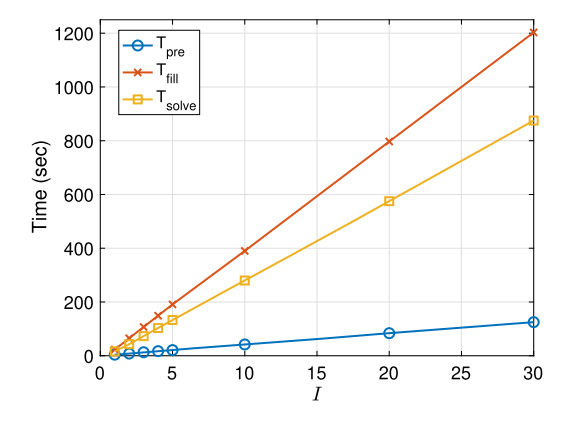


Fig. 5. Linear scaling of computational times from Table 1.

parameters, if not specified, are fixed at $N=120^2$, $M_{\rm w}=M=25^2$, P=3120. Quadrature corrections of $7^{\rm th}$ order are used. For both the flux error and the point-wise error of the field, we observe $7^{\rm th}$ order convergence with respect to the grid spacing (i.e., the error is $O(\sqrt{N})^{-7}$) and super-algebraic convergence with respect to the number of proxy points P.

In Fig. 4, we perform additional convergence study similar to Fig. 3 by changing the level of roughness of the interface and the order of quadrature correction. As expected, we observe that a higher order method (7^{th} order) converges faster and provides more digits of accuracy than a lower order method (5^{th} order) at the same number of discretization points. When the interface is a highly corrugated (h = 0.5), more points (larger N) are required than a less corrugated interface (h = 0.2) to reach the same level of accuracy. In the middle panel of Fig. 4, the slope of the convergence plot is 2.5 for 5^{th} order and 3.5 for 7^{th} order (before they reach a plateau of 10 digits of accuracy), since the order of accuracy of the method is with respect to the grid spacing, which is $O(N^{-1/2})$.

Computational time and memory requirement With the sparse system (47), the required computational time and memory are expected to scale *linearly* against the number of interfaces I. In Table 1, we show the computational results for media with 1 to 30 interfaces, where T_{pre} is the time for precomputing the quadrature correction weights, T_{fill} the time and M_{fill} the memory required for filling the matrices in the system (17)-(19), and T_{solve} the total time for both the reduction to and the solution of the block tridiagonal system (47) via block LU factorization. In all cases, the interfaces Γ_i are parameterized by $g_i(x,y) = 0.2 \sin(2\pi x) \cos(2\pi y) - (i-1)$ and discretized using $N = 60^2$ points each and with T^{th} -order quadrature. The wavenumbers k_i alternate between 10 and 20. Other parameters are fixed at $\phi^{\text{inc}} = 5\pi/6$, $\theta^{\text{inc}} = \pi/4$, P = 2380, $M_w = M = 20^2$ and K = 10. The relative flux error stays below 5×10^{-6} for

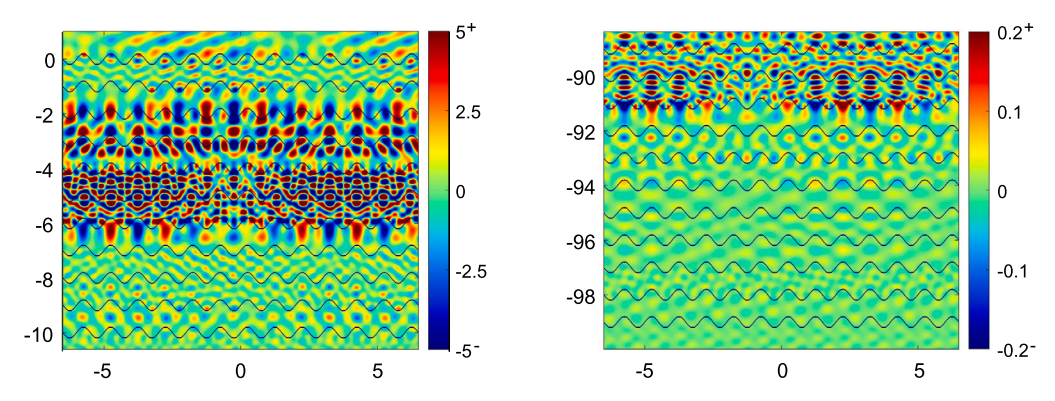


Fig. 6. 101-layered media scattering. The left panel shows the real part of the total field in the top 12 layers and the right panel in the bottom 12 layers (note the different color scales). The wavenumbers for each layer are chosen randomly in [8,20]. $N=60^2$ points per interface and P=2380 proxy points per layer are used. Computation is done in 1.83 hours and requires 321 GB of RAM. Relative flux error $\sim 7.4 \times 10^{-5}$.

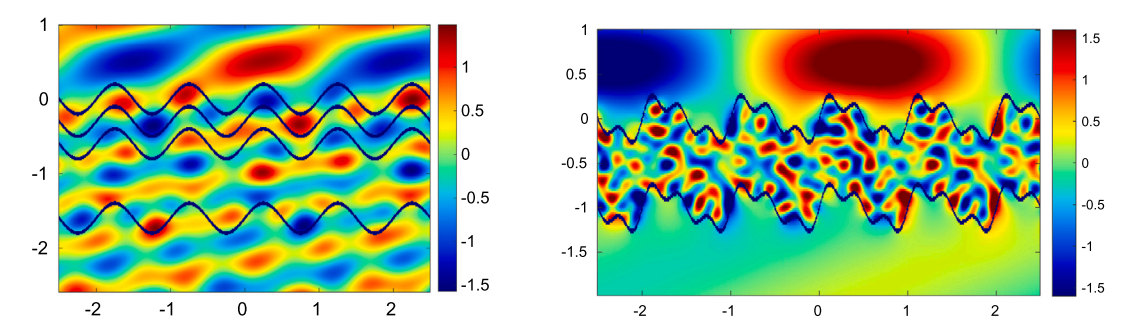


Fig. 7. Left panel: A five-layered media with two thin layers. The thickness is 0.3 for the thin layers and is 1 for the other layers. The wavenumbers for each layer are 5, 10, 8, 12, 10. The rest of the parameters are the same as in Fig. 6. Relative flux error is 8.8×10^{-8} . **Right panel**: A three-layered media with more complex surfaces and high-contrast layers, where the wavenumbers of the three layers are 3, 30, 3 (a 1-to-10 contrast). A 140×140 mesh is used for each interface and P = 4900 proxy points for each layer, the flux error is 5.5×10^{-4} .

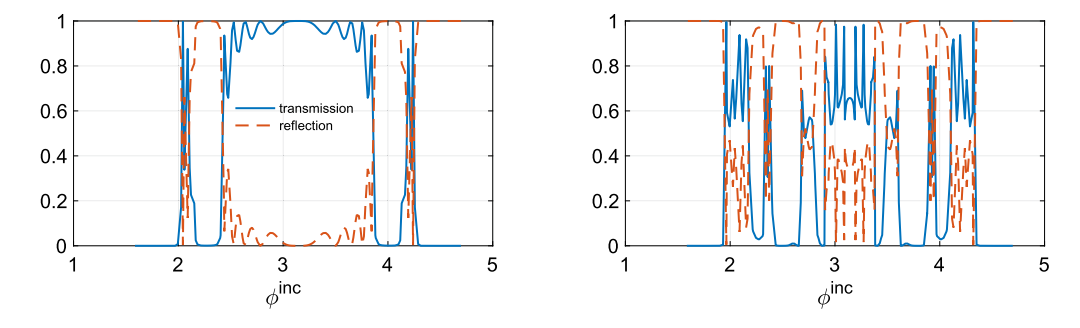


Fig. 8. The transmission and reflection spectra of an 11-layered media, where the wavenumbers k_i of each layer alternates between 2π and 4π . Left panel: spectra for h = 0 (flat interfaces). Right panel: spectra for h = 0.2 (corrugated interfaces).

any number of layers presented. The timing data in Table 1 is also plotted in Fig. 5, which clearly demonstrates a linear scaling of the computational times with respect to the number of interfaces *I*.

Example with 101 layers To demonstrate the capability of the algorithm, Fig. 6 shows the total field across a 101-layered media (cross-section in the xz-plane). The wavenumbers k_i are randomly chosen between 8 and 20 for each layer. A relative flux error of 7.4×10^{-5} is achieved with the parameters $N = 60^2$, P = 2380, $M_w = M = 20^2$, K = 10, and with 7th order quadrature corrections. The total number of unknowns is about 961.3k. The computation is completed in about 1.83 hours (0.2 hours for precomputing the quadrature correction weights, 1.28 hours for filling the matrices and 0.35 hours for solving the system) and used about 321 GB of memory.

Scattering in more complex layered media The next two examples illustrates the flexibility of our solver in handling more complex media. The left panel of Fig. 7 shows a plane wave through a five-layered media with layers of disparate thickness, where the middle layers Ω_2 and Ω_3 (both have a thickness of 0.3) are thinner than the layer Ω_4 (whose thickness is 1). In practice, this geometry may

correspond to two layers of thin coating on a given material. One distinctive feature of this example is that, for the thin layer Ω_2 (and likewise Ω_3), the lowest point of the upper interface Γ_1 is below the highest point of the lower interface Γ_2 . On the other hand, the right panel of Fig. 7 presents a three-layered media with high-contrast layers and more deformed interfaces. The wavenumbers of the three layers are $k_1 = 3$, $k_2 = 30$ and $k_3 = 3$, giving a 1-to-10 contrast across the interfaces. The two interfaces are each described by the formula $z = 0.2 \sin(2\pi x) \cos(2\pi y) + 0.05 \sin(4\pi x) \cos(4\pi y) + 0.1 \sin(6\pi x) \cos(6\pi y)$ and are separated by a distance of 1. Using a 140×140 mesh on each interface and P = 4900 proxy points for each layer, the solution has a flux error of 5.5×10^{-4} .

Transmission and reflection spectra Finally, we compute the transmission and reflection spectra, for a range of incident angles $\pi/2 < \phi^{\rm inc} < 3\pi/2$ and fixed $\theta^{\rm inc} = 0$, for an 11-layered media with flat or corrugated interfaces. Γ_i are parameterized by $g_i(x,y) = h\sin(2\pi x)\cos(2\pi y) - (i-1)$ for $1 \le i \le 10$. In Fig. 8, we show the spectra for h=0 (flat interfaces) and h=0.2 (corrugated interfaces). The wavenumbers k_i alternate between 2π and 4π (i.e., alternating between 1 and 2 wavelengths across layers). We used $N=40^2$ points for each interface and P=1740 proxy points for each layer, so that the flux error is below 10^{-4} in all cases for all incident angles. We observe that when the interfaces are corrugated, the spectra vary faster with the incident angle than when the interfaces are flat. The computations are accelerated by precomputing and storing the matrix components that are independent of the incident angle or the Bloch phases, at the cost of higher memory requirements. In Fig. 8, a total of 300 incident angles are considered in each case, with 150 independent angles (due to symmetry) and 100 independent Bloch phases. For h=0 (or h=0.2), it takes 103 seconds (or 116 seconds) to precompute and store the matrices independent of the incident angles, then 3770 seconds (or 3980 seconds) to solve the systems for all the independent phases, this gives an estimate of over 4x speedup compared to an unaccelerated computation.

5. Conclusion

A new 3-D multilayered media solver for doubly periodic geometry is presented. The solver is fast, accurate, and robust, equipped with new high-order specialized quadrature. An accuracy of 5 to 10 digits can be obtained for structures with multiple smooth layers with a small number of unknowns for each interface. The solver is capable of handling a structure with 101 layers in under 2 hours. The computational time and the memory requirement scale linearly with the number of layers in the structure. The transmission and reflection spectra for media with many layers can be computed efficiently, which is useful for applications in science and engineering. Future directions include extending our method to handle non-smooth layers using clustered nodes or panel-based quadratures (such as [56]), further accelerating the present solver by developing fast direct solvers in the style of [29], and developing new solvers for Maxwell's equations.

CRediT authorship contribution statement

Bowei Wu: Conceptualization, Methodology, Software, Validation, Writing – original draft, Writing – review & editing. **Min Hyung Cho:** Conceptualization, Methodology, Supervision, Validation, Writing – original draft, Writing – review & editing.

Declaration of competing interest

The authors declare that they have no known competing financial interests or personal relationships that could have appeared to influence the work reported in this paper.

Data availability

The Matlab source code can be found at https://github.com/bobbielf2/ZetaTrap3D_Unified.

Acknowledgement

This work was supported by the National Science Foundation (NSF-DMS 2012382). B. Wu thanks Per-Gunnar Martinsson for generously allowing use of his workstation for the 101-layered media example. M.H. Cho and B. Wu thank Alex Barnett for his help to identify the collaboration for this work.

References

- [1] M. Perry, R. Boyd, J. Britten, D. Decker, B. Shore, C. Shannon, E. Shults, High-efficiency multilayer dielectric diffraction gratings, Opt. Lett. 20 (8) (1995) 940–942.
- [2] C. Barty, M. Key, J. Britten, et al., An overview of llnl high-energy short-pulse technology for advanced radiography of laser fusion experiments, Nucl. Fusion 44 (12) (2004) S266.
- [3] H.A. Atwater, A. Polman, Plasmonics for Improved Photovoltaic Devices, Materials for Sustainable Energy: A Collection of Peer-Reviewed Research and Review Articles from Nature Publishing Group, 2011, pp. 1–11.
- [4] M.D. Kelzenberg, S.W. Boettcher, J.A. Petykiewicz, D.B. Turner-Evans, M.C. Putnam, E.L. Warren, J.M. Spurgeon, R.M. Briggs, N.S. Lewis, H.A. Atwater, Enhanced absorption and carrier collection in si wire arrays for photovoltaic applications, Nat. Mater. 9 (3) (2010) 239–244.
- [5] A.P. Raman, M.A. Anoma, L. Zhu, E. Rephaeli, S. Fan, Passive radiative cooling below ambient air temperature under direct sunlight, Nature 515 (7528) (2014) 540–544.

- [6] J.D. Joannopoulos, S.G. Johnson, R.D. Meade, J.N. Winn, Photonic Crystals: Molding the Flow of Light, 2nd edition, Princeton Univ. Press, Princeton, NJ, 2008.
- [7] B.T. DeBoi, A.N. Lemmon, B. McPherson, B. Passmore, Improved methodology for parasitic analysis of high-performance silicon carbide power modules, IEEE Trans. Power Electron. 37 (10) (2022) 12415–12425.
- [8] B. Kim, H. Jeon, D. Park, G. Kim, N.-H. Cho, J. Khim, Emi shielding leadless package solution for automotive, J. Adv. Join. Process. 5 (2022) 100102.
- [9] R. Model, A. Rathsfeld, H. Gross, M. Wurm, B. Bodermann, A scatterometry inverse problem in optical mask metrology, J. Phys. Conf. Ser. 135 (2008) 012071.
- [10] I.C. Tsantili, M.H. Cho, W. Cai, G.E. Karniadakis, A computational stochastic methodology for the design of random meta-materials under geometric constraints, SIAM J. Sci. Comput. 40 (2) (2018) B353–B378.
- [11] A. Taflove, S.C. Hagness, M. Piket-May, Computational electromagnetics: the finite-difference time-domain method, Electr. Eng. Handb. 3 (2005) 629-670.
- [12] G. Bao, Finite element approximation of time harmonic waves in periodic structures, SIAM J. Numer. Anal. 32 (4) (1995) 1155-1169.
- [13] P. Monk, et al., Finite Element Methods for Maxwell's Equations, Oxford University Press, 2003.
- [14] Y. He, M. Min, D.P. Nicholls, A spectral element method with transparent boundary condition for periodic layered media scattering, J. Sci. Comput. 68 (2) (2016) 772–802
- [15] M. Moharam, T. Gaylord, Rigorous coupled-wave analysis of planar-grating diffraction, J. Opt. Soc. Am. 71 (7) (1981) 811–818.
- [16] L. Li, Use of Fourier series in the analysis of discontinuous periodic structures, JOSA A 13 (9) (1996) 1870-1876.
- [17] M.H. Cho, Y. Lu, J.Y. Rhee, Y.P. Lee, Rigorous approach on diffracted magneto-optical effects from polar and longitudinal gyrotropic gratings, Opt. Express 16 (21) (2008) 16825–16839.
- [18] D.P. Nicholls, Method of field expansions for vector electromagnetic scattering by layered periodic crossed gratings, J. Opt. Soc. Am. A 32 (5) (2015) 701–709.
- [19] Y. Hong, D.P. Nicholls, A high-order perturbation of surfaces method for vector electromagnetic scattering by doubly layered periodic crossed gratings, J. Comput. Phys. 372 (2018) 748–772.
- [20] O.P. Bruno, M. Lyon, C. Pérez-Arancibia, C. Turc, Windowed Green function method for layered-media scattering, SIAM J. Appl. Math. 76 (5) (2016) 1871–1898.
- [21] O.P. Bruno, C. Pérez-Arancibia, Windowed Green function method for the Helmholtz equation in the presence of multiply layered media, Proc. R. Soc. A, Math. Phys. Eng. Sci. 473 (2202) (2017) 20170161.
- [22] C. Pérez-Arancibia, S.P. Shipman, C. Turc, S. Venakides, Domain decomposition for quasi-periodic scattering by layered media via robust boundary-integral equations at all frequencies, Commun. Comput. Phys. 26 (2019) 265–310.
- [23] D.P. Nicholls, C. Pérez-Arancibia, C. Turc, Sweeping preconditioners for the iterative solution of quasiperiodic Helmholtz transmission problems in layered media. J. Sci. Comput. 82 (2) (2020) 1–45.
- [24] M.H. Cho, W. Cai, A parallel fast algorithm for computing the Helmholtz integral operator in 3-d layered media, J. Comput. Phys. 231 (17) (2012) 5910-5925.
- [25] D. Chen, M.H. Cho, W. Cai, Accurate and efficient nystrom volume integral equation method for electromagnetic scattering of 3-d metamaterials in layered media, SIAM J. Sci. Comput. 40 (1) (2018) B259–B282.
- [26] J. Lai, M. Kobayashi, L. Greengard, A fast solver for multi-particle scattering in a layered medium, Opt. Express 22 (17) (2014) 20481–20499.
- [27] M.H. Cho, A.H. Barnett, Robust fast direct integral equation solver for quasi-periodic scattering problems with a large number of layers, Opt. Express 23 (2) (2015) 1775–1799.
- [28] Y. Zhang, A. Gillman, A fast direct solver for two dimensional quasi-periodic multilayered media scattering problems, BIT Numer. Math. 61 (1) (2021) 141–171.
- [29] Y. Zhang, A. Gillman, A fast direct solver for two dimensional quasi-periodic multilayered media scattering problems, Part II, arXiv preprint, arXiv:2204.06629, 2022.
- [30] M.H. Cho, Spectrally-accurate numerical method for acoustic scattering from doubly-periodic 3D multilayered media, J. Comput. Phys. 393 (2019) 46-58.
- [31] A. Boag, Y. Leviatan, A. Boag, Analysis of three-dimensional acoustic scattering from doubly periodic structures using a source model, J. Acoust. Soc. Am. 91 (2) (1992) 572–580
- [32] L. Greengard, V. Rokhlin, A fast algorithm for particle simulations, J. Comput. Phys. 73 (2) (1987) 325–348.
- [33] V. Rokhlin, Rapid solution of integral equations of scattering theory in two dimensions, J. Comput. Phys. 86 (2) (1990) 414-439.
- [34] M.H. Cho, W. Cai, A wideband fast multipole method for the two-dimensional complex Helmholtz equation, Comput. Phys. Commun. 181 (12) (2010) 2086–2090.
- [35] W. Hackbusch, A sparse matrix arithmetic based on H-matrices. Part I: introduction to H-matrices, Computing 62 (2) (1999) 89–108.
- [36] P.-G. Martinsson, V. Rokhlin, A fast direct solver for boundary integral equations in two dimensions, J. Comput. Phys. 205 (1) (2005) 1–23.
- [37] L. Greengard, D. Gueyffier, P.-G. Martinsson, V. Rokhlin, Fast direct solvers for integral equations in complex three-dimensional domains, Acta Numer. 18 (2009) 243–275.
- [38] S. Börm, Efficient Numerical Methods for Non-local Operators: H2-Matrix Compression, Algorithms and Analysis, vol. 14, European Mathematical Society, 2010.
- [39] J. Xia, S. Chandrasekaran, M. Gu, X.S. Li, Fast algorithms for hierarchically semiseparable matrices, Numer. Linear Algebra Appl. 17 (6) (2010) 953–976.
- [40] J.-Q. Wang, Z.-D. Zhang, S.-Y. Yu, H. Ge, K.-F. Liu, T. Wu, X.-C. Sun, L. Liu, H.-Y. Chen, C. He, et al., Extended topological valley-locked surface acoustic waves, Nat. Commun. 13 (1) (2022) 1324.
- [41] G. Ma, P. Sheng, Acoustic metamaterials: from local resonances to broad horizons, Sci. Adv. 2 (2) (2016) e1501595.
- [42] Y. Liu, A.H. Barnett, Efficient numerical solution of acoustic scattering from doubly-periodic arrays of axisymmetric objects, J. Comput. Phys. 324 (2016) 226–245
- [43] B. Wu, P.-G. Martinsson, Zeta correction: a new approach to constructing corrected trapezoidal quadrature rules for singular integral operators, Adv. Comput. Math. 47 (3) (2021) 1–21
- [44] B. Wu, P.-G. Martinsson, Corrected trapezoidal rules for boundary integral equations in three dimensions, Numer. Math. 149 (4) (2021) 1025–1071.
- [45] B. Wu, P.-G. Martinsson, A unified trapezoidal quadrature method for singular and hypersingular boundary integral operators on curved surfaces, arXiv preprint, arXiv:2209.02150, 2022.
- [46] B.H. Kleemann, Fast integral methods for integrated optical systems simulations: a review, in: Optical Systems Design 2015: Computational Optics, vol. 9630, 2015, pp. 119–137.
- [47] R.W. Wood, XLII. On a remarkable case of uneven distribution of light in a diffraction grating spectrum, Philos. Mag. 4 (21) (1902) 396-402.
- [48] D.L. Colton, R. Kress, R. Kress, Inverse Acoustic and Electromagnetic Scattering Theory, vol. 93, Springer, 1998.
- [49] A.-S. Bonnet-Bendhia, F. Starling, Guided waves by electromagnetic gratings and non-uniqueness examples for the diffraction problem, Math. Methods Appl. Sci. 17 (5) (1994) 305–338.
- $\textbf{[50]} \ \ \textbf{C. Linton, I. Thompson, Resonant effects in scattering by periodic arrays, Wave Motion 44 (3) (2007) 165-175.$
- [51] A. Barnett, L. Greengard, A new integral representation for quasi-periodic scattering problems in two dimensions, BIT Numer. Math. 51 (2011) 67–90.
- [52] S.P. Shipman, Resonant scattering by open periodic waveguides, Prog. Comput. Phys. 1 (2010) 7–49.
- [53] A. Barnett, L. Greengard, A new integral representation for quasi-periodic fields and its application to two-dimensional band structure calculations, J. Comput. Phys. 229 (19) (2010) 6898–6914.
- [54] J. Lyness, An error functional expansion for n-dimensional quadrature with an integrand function singular at a point, Math. Comput. 30 (133) (1976) 1–23.
- [55] G.H. Golub, C.F. Van Loan, Matrix Computations, 3rd edition, The Johns Hopkins University Press, 1996.
- [56] J. Bremer, Z. Gimbutas, A Nyström method for weakly singular integral operators on surfaces, J. Comput. Phys. 231 (14) (2012) 4885-4903.